Int. J. Electrochem. Sci., 13 **(2018)** 1105 – 1119, doi: 10.20964/2018.01.75

International Journal of
ELECTROCHEMICAL
SCIENCE
www.electrochemsci.org

The Electrochemical Dissolution Characteristics of GH4169 Nickel Base Super Alloy in the Condition of Electrochemical Machining

Yu Tang, Zhengyang Xu[*]

College of Mechanical and Electrical Engineering, Nanjing University of Aeronautics and Astronautics, Nanjing, 210016, China
[*] E-mail: xuzhy@nuaa.edu.cn

Received: 27 June 2017 / *Accepted:* 18 November 2017 / *Published:* 16 December 2017

The nickel-based super-alloy of GH4169 is often used for manufacturing core functional components of turbo-machinery systems. It is a kind of high temperature, high specific strength and wear-resistant material, and machining this material by the use of conventional means is difficult. Electrochemical machining (ECM) is an effective method to machine GH4169 alloys but the electrochemical dissolution characteristics of GH4169 under ECM conditions are different from those measured by conventional electrochemical measurements. This study focuses on the electrochemical dissolution characteristics of GH4169 under ECM conditions. The open circuit potential, electrochemical impedance spectrum (EIS) and anodic polarization curve are investigated. The polarization curves were measured using an electrochemical workstation and corresponding equations were obtained by computer fitting. In addition, a formula for the electrochemical polarization resistance and the peak phase of alternating-current impedance's Bode diagram is deduced, and surface defects arising from unsteady flow in different electrolyte are compared.

Keywords: Electrochemical machining; GH4169; Electrochemical dissolution

1. INTRODUCTION

The GH4169 nickel-base super-alloy is commonly used to produce aerospace engines and gas turbine wheels, blades, and other heat-resistant parts, because of its excellent thermal strength, stability, and fatigue performances at high temperature [1–3]. However, it is challenging to machine such 'difficult-to-cut' materials using conventional means, often resulting in low material removal rates, reduced precision because of high cutting forces, high tooling costs, and low process efficiency [4–6]. In addition, the resulting surface integrity is often characterized by thermo-mechanically altered or

even damaged rim zones. In order to overcome the current manufacturing limitations of conventional machining, electrochemical machining (ECM) is often required for machining such alloys [7–9].

Research into anodic electrochemical dissolution characteristics is a precondition of ECM. However, the electrolyte of conventional electrochemical measurements undergoes free convection, and the electrode gap between the working electrode and counter electrode is several millimetres, where only a low exchange current (current density 0–100 mA/cm²) can be measured by the use of a three-electrode system [10–12]. Actually there is high speed flow of electrolyte (6–30 m/s), high current density (10–100 A/cm ²), and small electrode gap (0.1–1 mm) in ECM [7, 13, 14]. Therefore, conventional electrochemical measurement conditions do not correspond to the electrochemical machining requirements, and the open circuit potential, electrochemical impedance spectra and linear sweep voltammetry curves obtained by the former do not correspond to the dissolution characteristic of ECM actually; thus, it is necessary to carry out the detection and analysis of electrochemical dissolution characteristics curve under ECM conditions.

In recent years, many researchers have focused on the ECM and the electrochemical dissolution characteristics of 'difficult-to-cut' materials, especially nickel-base super-alloy. Ching used a rotating disc electrode to study the electrochemical dissolution behaviour of Inconel 718 in perchloric-acetic acid mixtures and identified chose a suitable electrolyte to polish Inconel 718 [15]. Wang carried out basic research on stray corrosion of Inconel 718 and 304 stainless steel in $NaNO_3$ solution [16]. Qu conducted basic research on electrochemical grinding of Inconel 718 [17]. Singh analysed the microstructural and carried out multi-response optimisation during the ECM of Inconel 825 [18]. Wynick used electro-polishing to enhance Inconel 718 and Ti-22Al-28Nb preparation for electron backscatter diffraction analysis [19]. Kalaimathi performed experiments on the electrochemical machining characteristics of Monel 400 Alloys and optimised the process parameters [20]. Gu evaluated the flow field in the electrochemical trepanning of aero engine diffuser which was made of nickel-based super alloy [21]. Jain employed jet-electrochemical micromachining to produce micro-hole patterns on Incoloy 800 specimens [22]. In addition to these, Weinmann investigated electrochemical dissolution behaviors of Ti90Al6V4 and Ti60Al40 used for ECM applications [23].

To test the dissolution characteristics of GH4169 under ECM conditions, an experimental testing device has been designed and set up. This study focuses on analysing the time–voltage curves, electrochemical impedance spectra, and linear sweep voltammetry curves of GH4169 measured under ECM conditions, and comparing with those measured under conventional electrochemical conditions. By analysing the electrochemical impedance spectra, a formula for the electrochemical polarization resistance and the peak phase of alternating-current impedance's Bode diagram was deduced. The surface qualities of the work-pieces which were manufactured by ECM, had different characteristics in different electrolyte. The results show that the decay resistance of GH4169 under ECM conditions is lower than that under conventional electrochemical measurement conditions and that there was no pre-passivation because of the high-speed flowing electrolyte. In addition, the surfaces of GH4169 were more likely to have lower processing quality because of the unsteady flow in sodium chloride aqueous solution, whose electrochemical activity and volume expansion ratio of anodic products were higher than those in sodium nitrate aqueous solution.

2. EXPERIMENTAL

2.1. Testing environment

An experimental testing system, which consists of a three-electrode system [24], testing device, and electrolyte circulation system, has been designed and set up. Among these, the electrolyte circulation system, which contains a fixture, temperature sensor, flow-meter, filter, throttling valve, centrifugal pump, thermostat bath, and counterbalance valve, can control the gap between electrodes, the flow velocity, and the temperature of the electrolyte, allowing the testing conditions to match to those of ECM. The structure of the experimental testing system is shown in Fig. 1.

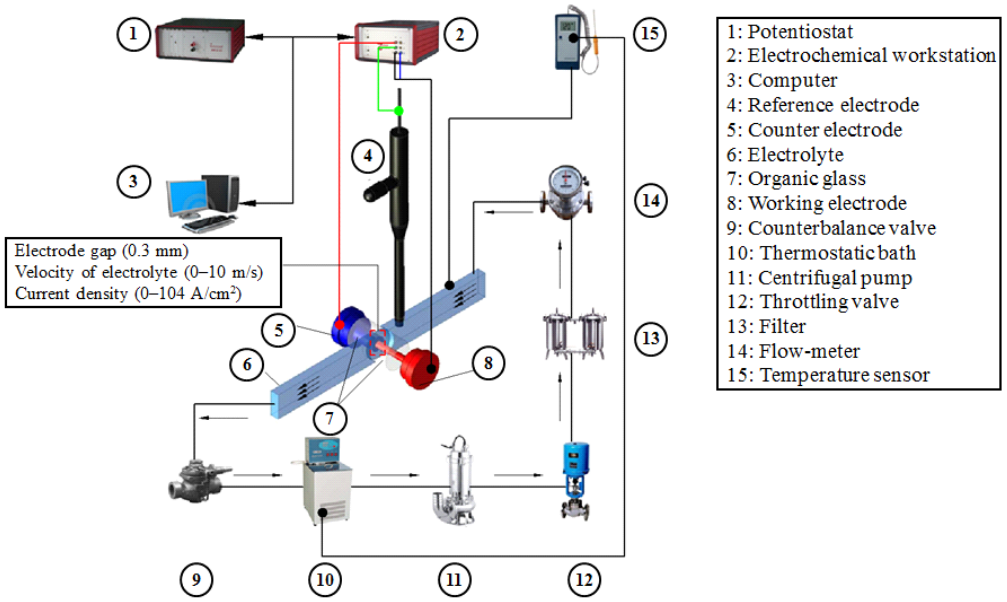

Figure 1. Structure of the experiment testing system

2.2. Materials and electrolytes

The work-piece material (the working electrode) is GH4169 alloy, which was produced with radial forging technology. The GH4169 alloy is a kind of precipitation hardened nickel-base super-alloy that is highly resistant to oxidation and corrosion because of the presence of Cr, Si, Mn, and Ti. Fig. 2 shows the geometry of the working electrode, isolated by an organic glass, whose working face is a 3.5 mm diameter circle. The schematic of the working electrode pre-processing is shown in Fig. 3. First, wire-cut electrical discharge machining (WEDM) was applied to obtain a cylindrical work-blank from a hunk of the GH4169 alloy. Next, high-speed turning was implemented to obtain a specimen with three different column sizes, where the smallest column was used as the working electrode and the largest column was used as locating feature to cut the insulating material into a cylindrical. Then, the organic glass was mixed and solidified, acting as the insulating material of the working electrode. Subsequently, excess organic glass was removed by turning, where the largest column of the specimen was the locating feature that ensured the size of the insulating material and its concentricity. In addition, the end face of organic glass was also cut by turning to expose the working electrode to the

air. The position plane was the end face of the largest column, ensuring that the electrode gap between the working electrode and the counter electrode was 0.3 mm.

Two types of electrolyte were used, sodium chloride and sodium nitrate electrolytes, both of which are widely used in the ECM industry. The electrolyte concentrations were both 1.84 mol/L. Distilled water was used to prepare these solutions, and the electrolyte circulation system was cleaned when we changed the electrolyte. The temperature of the electrolyte was maintained by the combination of a thermostatic bath and temperature sensor, and the velocity of the electrolyte was controlled by the combination of centrifugal pump, throttling valve, and flow-meter. In addition, a filter was used to remove the anodic products from the electrolyte, and a counterbalance valve was used to prevent the formation of a liquid deficient region in the gap between working-electrode and counter-electrode (Fig. 1).

Figure 2. Working electrode protected by organic glass

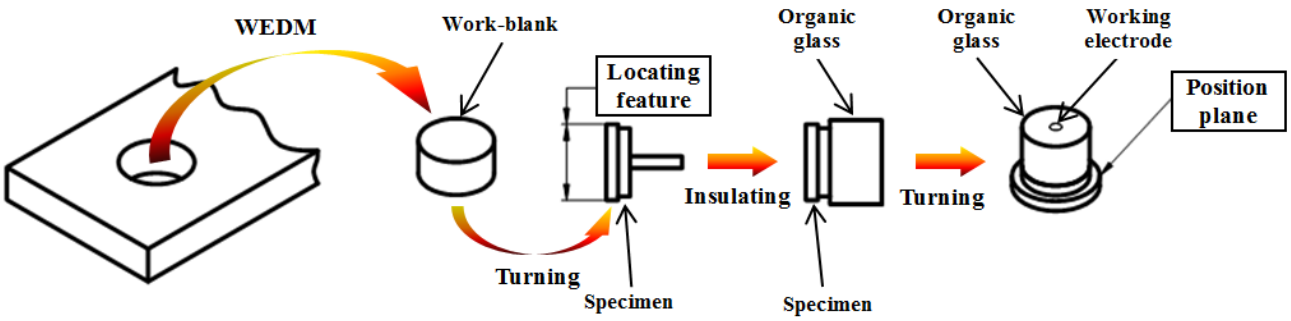

Figure 3. Schematic of the working electrode pre-processing

2.3. Experimental set-up and sample preparation

The components of the samples used in the study were characterised by energy-dispersive X-ray spectroscopy (EDX X-flash 5010, Bruker, Germany). Electrochemical measurements were performed using an electrochemical workstation and a potentiostat (Zennium E, Zahner Instruments Inc., Germany). The counter electrode was a platinum electrode, the reference electrode was a saturated calomel electrode (SCE), and the working face of the working electrode was pretreated using wet abrasive papers followed by rinsing with distilled water. All the anodic polarization curves tests were performed potentio-dynamically with a scan rate of 1 mV/s^{-1}, from 0 to 16 V. The

electrochemical impedance spectra (EIS) were recorded at 0 A/cm^{-2} and the frequency range during the EIS measurements was 100 kHz to 0.5 Hz. The open circuit potential curves were recorded at 0 A/cm^{-2}, from 0 to 15 min. The surface geometry of work-piece machined by ECM was characterized by a microscope (LEICA DVM5000, Leica, Germany).

3. RESULTS AND DISCUSSION

3.1. Composition of material samples

The principal composition of the GH4169 alloy samples was determined by EDX, as shown in Table 1.

Table 1. Composition of sample

Element	Cr	Si	Mn	Ti	Al	Ni	Fe	Nb	Mo	C
Wt%	19.26	0.06	0.07	0.98	0.60	52.51	18.10	5.24	3.10	0.08

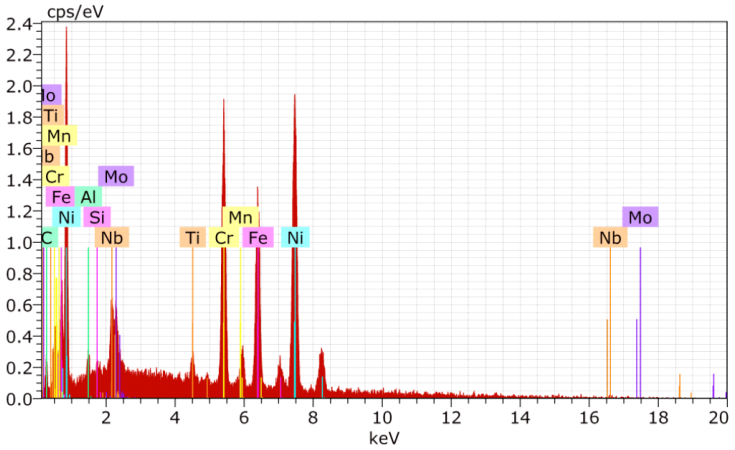

Figure 4. Energy dispersive X-ray spectrum of sample

3.2. Electrochemical characterization

3.2.1. The time dependence of open circuit potential curves

The time dependence of the open circuit potential (E_{OCP}) curves of GH4169 at 30 °C were measured under two conditions separately, including conventional electrochemical measurement condition, where the electrolyte is subject to free convection, and ECM conditions, where the primary clearance between working electrode and counter electrode is controlled to be 0.3 mm and the velocity of the electrolyte is controlled to be 10 m/s using the electrolyte circulation system. These two types of measurements were carried out in sodium chloride electrolyte and sodium nitrate electrolyte. The same molar concentration (1.84 mol/L) was used for both electrolytes. Thus, four E_{OCP} curves were

obtained, and these are shown in Fig. 5. The results show that the E_{OCP} values of GH4169 under ECM conditions are obviously lower than these in the condition of free convection because of the fast-flowing electrolyte. The E_{OCP} values of GH4169 in the sodium chloride electrolyte were lower than those in sodium nitrate electrolyte, regardless of the electrochemical conditions to which the GH4169 samples were subjected; this indicates that GH4169 is more easily to be fabricated by the use of electrochemical machining in sodium chloride electrolyte than in sodium nitrate electrolyte.

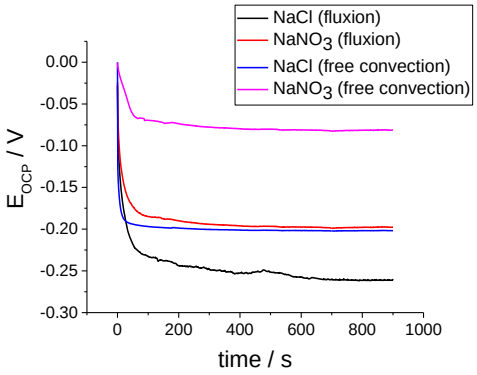

Figure 5. The time dependence of the E_{OCP} of GH4169 at 30 °C

3.2.2. The EIS studies and modelling of equivalent circuit

Fig. 6 shows the inverse Nyquist diagram of GH4169 at 30 °C. There is a semicircle in the high-frequency region and a straight line in the low-frequency impedance region, caused by the combination of the charge transfer and diffusion steps. Fig. 7(a) shows the equivalent circuit of the inverse Nyquist diagram. The ohmic resistance of the electrolyte, the capacitance of the electric double layer, the electrode reaction resistance, the resistance of concentration polarisation, and the capacitance of concentration polarisation are represented by the symbols R_1, C_d, R_r, R_w, and C_w, respectively. This equivalent circuit can be simplified when the frequency of the voltage (ω) is sufficiently high (ω > 100 Hz) because $R_w \propto \omega^{-0.5}$ and $C_w \propto \omega^{-0.5}$ [25]. The simplified equivalent circuit in the high frequency region is showed in Fig. 7(b). The data were evaluated using the equivalent circuits mentioned in Fig.7 (b), and the determined parameters are listed in Table 2, whose calculated fitting curves are shown in Fig.8 (solid lines).

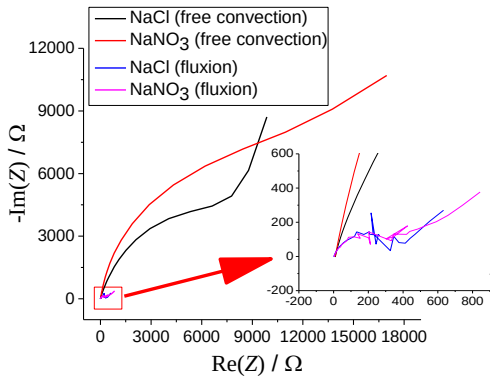

Figure 6. The inverse Nyquist diagram of GH4169 at 30 °C

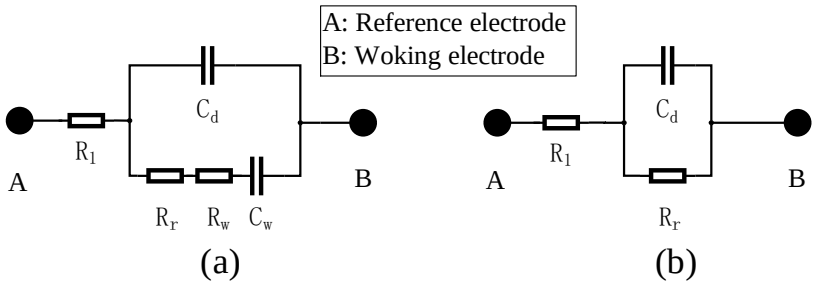

Figure 7. The equivalent circuit: (a) theoretical and (b) simplified circuit in the high frequency region

Table 2. Fitting results of the EIS measurements in the high-frequency region

Electrolyte	R_1 /Ω	C_d /μF	R_r /Ω
NaCl (free convection)	10.07	1.1044	4836
$NaNO_3$ (free convection)	11.42	1.4857	8326
NaCl (fluxion)	3.14	0.7161	211
$NaNO_3$(fluxion)	3.55	1.2757	193

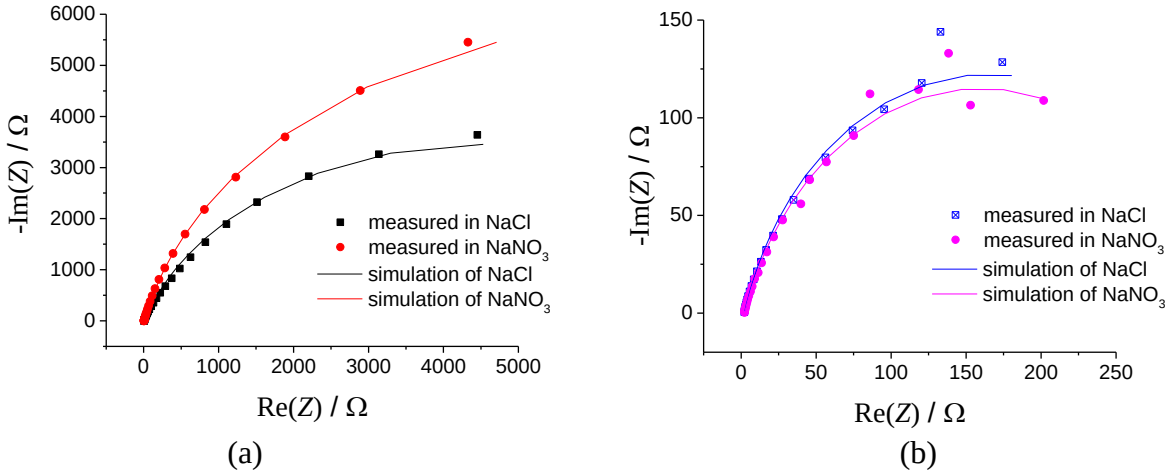

Figure 8. Measured data and calculated fitting curves of GH4169 in the high frequency region: (a) in free convection and (b) in fluxion

The impedance value of equivalent circuit in Fig. 7(b) can be expressed by equation:

$$Z = R_1 + \frac{R_r}{1 + j\omega R_r C_d} = R_1 + \frac{R_r}{1 + (\omega R_r C_d)^2} - j\frac{\omega R_r}{1 + (\omega R_r C_d)^2} \quad (1\text{-}1)$$

where Z is the impedance value between reference electrode and working electrode (Fig.7 (b)), R_1 represents the ohmic resistance of electrolyte, C_d represents the capacitance of electric double layer, R_r is the electrode reaction resistance, ω represents the frequency of voltage, and j is the square root of -1.

Because Z is a is complex number, the phase angle ($\varphi(\omega)$) of Z is given by:

$$\varphi(\omega) = arctan\frac{R_r^2 C_d \omega}{R_1 + R_r + R_1 R_r^2 C_d^2 \omega^2} \quad (1\text{-}2)$$

The maximum value of the phase angle (φ_{max}) and its corresponding value of voltage frequency (ω') are calculated as follows:

$$\varphi_{max} = \varphi\left(\frac{1}{R_r C_d}\sqrt{\frac{R_1+R_d}{R_1}}\right) = arctan\frac{R_r}{2\sqrt{R_1(R_1+R_r)}} \quad (1\text{-}3)$$

$$\omega' = \frac{1}{R_r C_d}\sqrt{\frac{R_1+R_d}{R_1}} \quad (1\text{-}4)$$

When the resistance of the electrolyte (R_1) is constant, the maximum value of the phase angle will increase with increasing electrode reaction resistance (R_r). Therefore, as the maximum value of the phase angle in the high-frequency region increases, the electrochemical activity of electrolyte decreases. The Bode diagrams of the GH4169 EIS measurements are shown in Fig. 9. In the phase-frequency curves of GH4169, the maximum values of the phase angle decrease, compared to those of free convection, as the speed of the high-speed flowing electrolyte increases. Therefore, the electrochemical activity of the electrolyte is increased by the flowing electrolyte, which indicates that flowing electrolyte is beneficial to the electron transfer process at the work-piece surface. This is the mechanism by which the fast-flowing electrolyte (10 m/s) reduces the E_{OCP} of GH4169 (Fig. 5).

In the GH4169 resistance-frequency curve, the impedance modulus of GH4169 in fluxion are decreased by two orders of magnitude at 0.5 Hz compared to that with free convection; this indicates that the flowing electrolyte is beneficial for ion diffusion and significantly reduces the concentration polarisation [20].

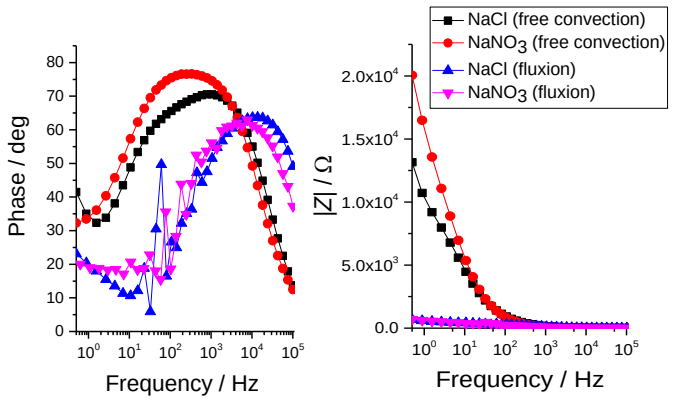

Figure 9. Bode diagrams of the GH4169 EIS measurements: the phase-frequency curve (left) and resistance-frequency curve (right)

3.2.3. Influence of the electrolyte velocity and temperature on the dissolution behaviour of the alloy

The anodic polarization curves of G4169 at 30 °C are shown in Fig. 10. The current densities in sodium nitrate electrolyte are always lower than those in sodium chloride electrolyte. This is because of the difference in the ion migration velocities between the electrolytes that results in the lower current density in the sodium nitrate electrolyte, where larger nitrate ions with larger relative ion mass migrate more slowly.

Ching have measured anodic polarization curves of the Inconel 718 in the HClO4–CH3COOH mixed acids with different HClO4-concentrations [28]. In their study, limiting-current plateaus were

detected in their anodic polarization curves, which were attributed to the dense mat film found on anode surface. Wang presented the passivation oxide film on the surface of Inconel 718, which influenced stray corrosion and current density of anode [16]. Compared to the state of free convection, the curves of fluxion are very different, and there are non-existent of pre-passivation region (the limiting-current plateau in Ching's study) after decomposition potential. This indicates that the shear stress generated in the interface between high-speed flowing electrolyte and anode wipes off the oxide layer of GH4169. When the electrolyte is free convection, the pre-passivation region in sodium chloride electrolyte is broader than that in sodium nitrate electrolyte. A possible explanation for this is that the volume expansion ratio of anodic products generated in sodium chloride electrolyte is greater than that in sodium nitrate electrolyte (105.47 in NaCl and 76.73 in $NaNO_3$), which leads to a higher trans-passive potential. With electrolyte flux, anodic polarization curves show a similar rising tendency in these two kinds of electrolyte because flow-field wipes off anodic products.

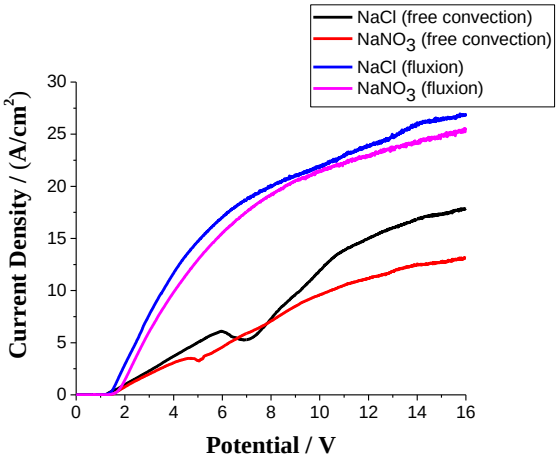

Figure 10. Polarization curves of GH4169 alloy

As what have been discussed in Fig. 9, a flowing electrolyte is beneficial for the electron transfer process at the work-piece surface and for the diffusion of metal ions from work-piece to electrolyte, thus fluxion increases the current densities. The polarization curves of GH4169 alloy at different velocities of electrolytes are shown in Fig. 11. The flow of the electrolyte is conducive to electrochemical machining, increasing current density and material removal rate, and further increasing the electrolyte velocity increases the current density.

Fig. 12 shows anodic polarization curves of GH4169 in flow field at different temperatures. The curves can be divided into two different regions. When anode potentials are below decomposition potentials, there is no electrochemical dissolution, and current densities are almost zero. When the potentials are above decomposition potentials, the current densities increase gradually, which means that electrochemical dissolution occurs. In sodium nitrate electrolyte, the decomposition potentials of GH4169 was located about 1.30 ± 0.05 V, whereas, in the sodium chloride electrolyte, the decomposition potential was 1.18 ± 0.05 V, which is lower than former because chloride ions with smaller sizes and stronger adsorptive properties can penetrate the oxide layer and react with the base

alloy more easily. In addition, in sodium nitrate electrolyte the current densities increase as the temperature rising from 30 to 50 °C, however, in the sodium chloride electrolyte, the current densities decreased with increasing temperature, from 40 to 50 °C.

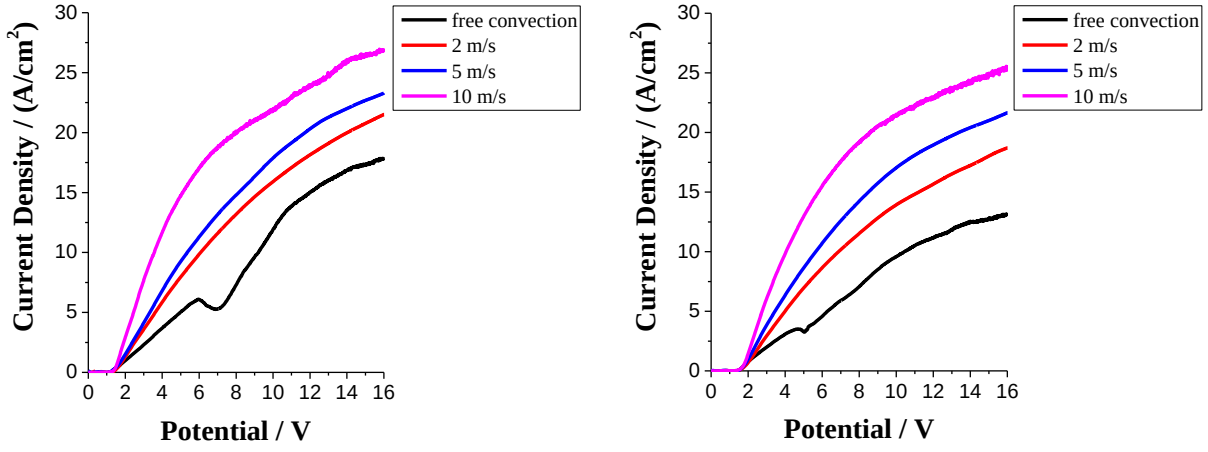

Figure 11. Polarization curves of GH4169 alloy at different velocities of electrolytes: (a) in NaCl and (b) in $NaNO_3$

These observations are explained in Fig. 13. As shown by equation (1-3), as the maximum value of the phase angle (φ_{max}) in the high-frequency region increases, the electrode reaction resistance (R_r) also increases; thus, the electrochemical activity of the electrolyte is reduced. In the sodium nitrate electrolyte, the electrochemical activities of the electrolytes increase and the impedance modulus decreases as the temperature increases; however, in the sodium chloride electrolyte, when the temperature increases from 40 to 50 °C, the electrochemical activities of electrolytes stay the same but the impedance modules increases, possibly because the increasing temperature resulted in the volume expansion of the anodic products, hindering metal ion diffusion from the anode to the electrolyte and electron transfer processes in the work-piece surface.

When the potentials were above decomposition potentials, the current densities (J) and anode potentials (Φ) fitted this equation:

$$J = a \times e^{b \times \Phi} + c \times \Phi + d \quad (1\text{-}5)$$

In this equation, a, b, c, and d are undetermined constants, and e Euler's number. The values of undetermined constants are shown in Table 3. In this table, the closer the coefficient of determination (R^2) is to 1, the better the fit of equation (1-5).

There is a turning point in each polarization curve when the potential is greater than the decomposition potential (Fig. 12). Here, the current density curve shows different characteristics on the two sides of this turning point; thus, we call this the turning potential (Φ_{tp}). In the sodium chloride electrolyte, Φ_{tp} is approximately 5 V, whereas, in the sodium nitrate electrolyte, Φ_{tp} is approximately 7 V (Fig. 12). When the anode potentials are lower than Φ_{tp}, the current densities increase exponentially with the anodic potential, whose two coefficients are constants of a and b. If the temperature rises, these two coefficients will change because of the change in the electrochemical reaction polarization

and concentration polarization. When the anode potential is sufficiently high (greater than Φ_{tp}), the current densities are linearly and positively correlated with the anode potential, whose positive correlation coefficient equals *c*. If the temperature rises, the coefficient of positive correlation increases because of the increased electrolyte conductivity.

Table 3. Undetermined constants of anodic polarization curves

Electrolyte	Temperature	*a*	*b*	*c*	*d*	R-square
1.84 mol/L NaCl fluxion(10 m/s)	30 °C	-29.99	-0.3619	0.6975	16.01	0.9989
	40 °C	- 50.59	- 0.5579	0.7060	20.53	0.9988
	50 °C	- 43.19	- 0.5131	0.7668	18.50	0.9984
1.84 mol/L $NaNO_3$ fluxion(10 m/s)	30 °C	- 33.18	- 0.2692	0.3837	19.78	0.9996
	40 °C	- 34.85	- 0.3274	0.6200	18.28	0.9992
	50 °C	- 37.77	- 0.3586	0.7716	18.89	0.9971

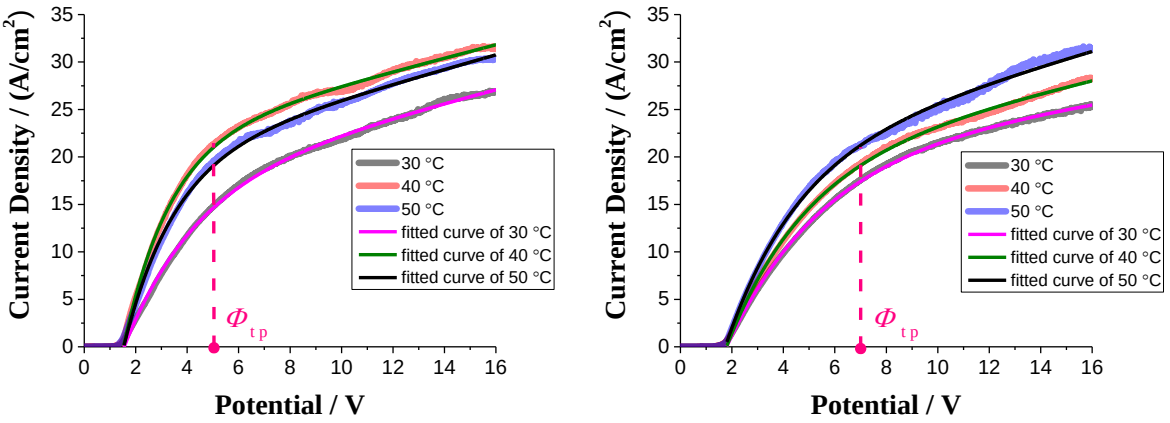

Figure 12. Polarization curves and fitted curves for GH4169 alloy in a flow field at different temperatures: (a) measured in sodium chloride electrolyte and (b) measured in sodium nitrate electrolyte

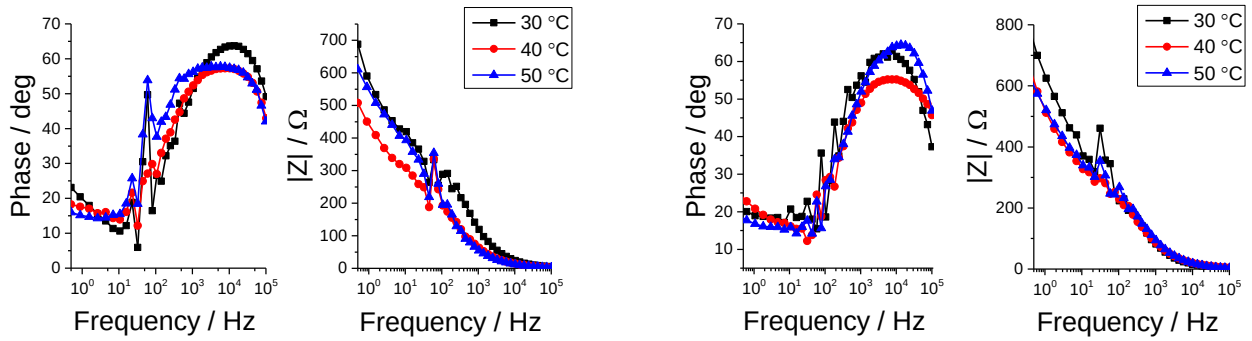

Figure 13. Bode diagrams for GH4169 alloy under ECM condition at different temperatures: (a) measured in sodium chloride electrolyte and (b) measured in sodium nitrate electrolyte

3.2.4. Influence of the electrolyte on work-piece surface quality

As discussed above, there are significant differences in the electrochemical dissolution characteristics of GH4169 between the sodium chloride electrolyte and sodium nitrate electrolyte. The surfaces of GH4169 alloy manufactured by ECM are also different (Figs. 14 and 15). In the sodium chloride electrolyte, the surfaces of GH4169 alloy have conspicuous sunken region on the left side of circular work-piece, whereas, in the sodium nitrate electrolyte, the work-piece surfaces are smoother.

Figure 14. Surfaces of GH4169 alloy in NaCl electrolyte at different temperatures

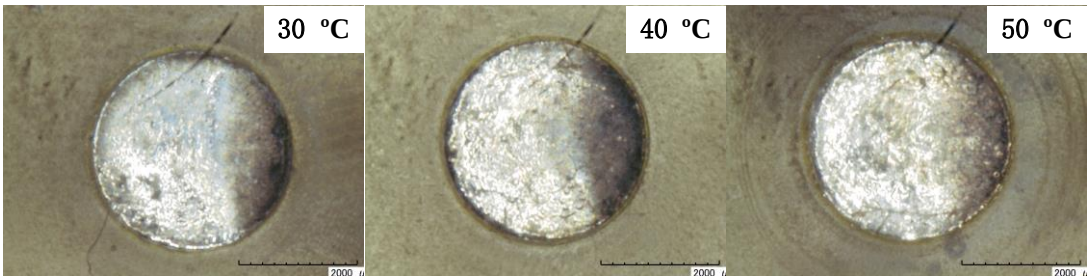

Figure 15. Surfaces of GH4169 alloy in $NaNO_3$ electrolyte at different temperatures

The simulation and analysis of the flow field were carried out using computational fluid dynamics (CFD) modelling, and the finite element method (FEM) discretization meshes of this mode are demonstrated in Fig. 16. The simulation boundaries are the following. 1) The volume flow rate of the inlet is 4.8 mL/s. 2) The outlet pressure is 0.1 MPa. The turbulence eddy dissipation of electrolyte based on the *k-e* turbulence model is shown in Fig. 17(a). Roode presented the parameterised equation for turbulent kinetic energy models [26]. This equation can be written as

$$\underbrace{\frac{\partial e}{\partial t}}_{\text{Tendency}} + \underbrace{u_j\frac{\partial e}{\partial x_j}}_{\text{Mean advection}} = \underbrace{-K_h N^2}_{\text{Buoyancy}} + \underbrace{K_m S^2}_{\text{Shear production}} + \underbrace{2\frac{\partial}{\partial x_j}\left(K_m\frac{\partial e}{\partial x_j}\right)}_{\text{Turbulent transport}} - \underbrace{\frac{c_\varepsilon e^{3/2}}{\lambda}}_{\text{Dissipation}} \quad (1\text{-}6)$$

with

$$S^2 \equiv \frac{1}{2}\left(\frac{\partial u_j}{\partial x_i}+\frac{\partial u_i}{\partial x_j}\right)^2 = \left(\frac{\partial u_j}{\partial x_i}+\frac{\partial u_i}{\partial x_j}\right)\frac{\partial u_i}{\partial x_j} \quad (1\text{-}7)$$

where e, t, and u are the typical kinetic energy, time, and velocity, and K_h, N, K_m, c_ε, and λ represent the eddy viscosity for momentum, buoyancy frequency, the eddy diffusivity for the thermodynamic scalars, the proportionality constant for molecular viscosity, and the characteristic

length scale of the turbulent eddies, respectively. In the viscous, turbulent flow-field, the large-scale turbulent eddies (λ are large) contribute to the transport of the fluid elements and the turbulence energy, and the small-scale turbulent eddies (λ are small) contribute to the adulteration of the fluid elements and the dissipation of turbulence energy [26–27]. As shown in Fig. 17(b), the distribution of electrolyte velocities are concentrated in low eddy dissipation region, where the size of turbulent eddies (λ in equation (1-6)) are small, however the distribution of electrolyte velocities are incompact in high eddy dissipation region, where the size of turbulent eddies are large. Besides, on the right side of anode surface, there is the low Reynolds number region where electrolyte flows very slowly and almost has no eddy turbulence.

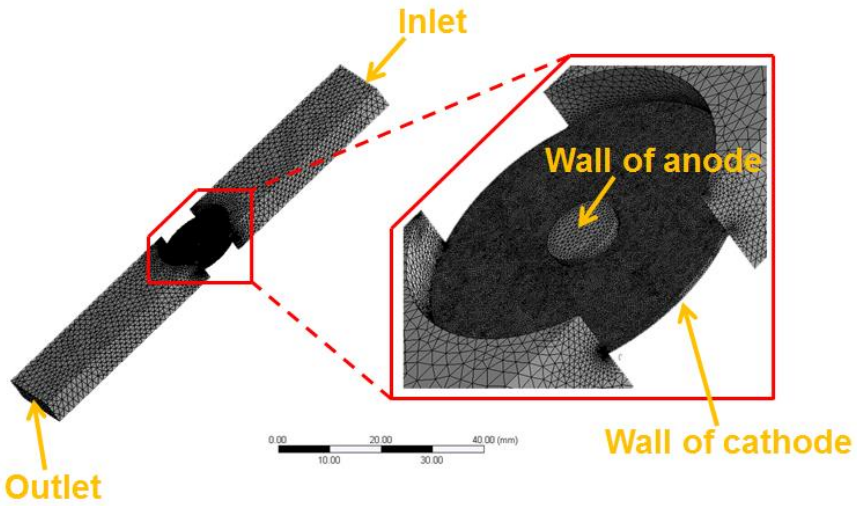

Figure 16. FEM discretization meshes of the electrolyte channel

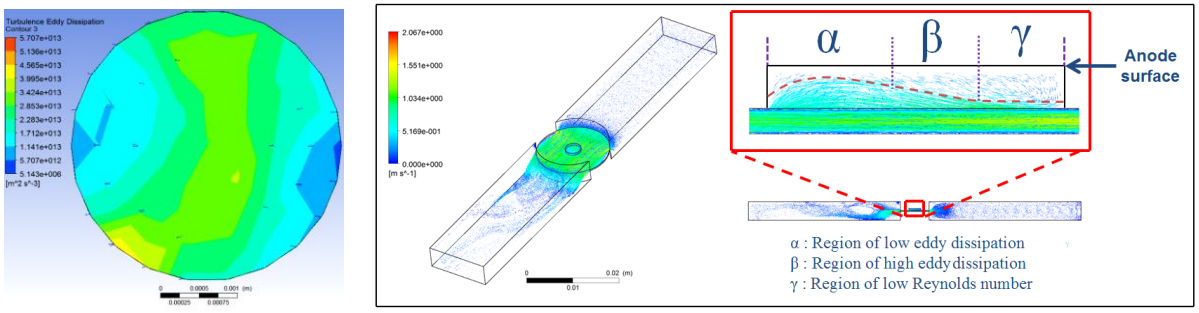

(a) (b)

Figure 17. Turbulent eddy dissipation of electrolyte (a) and electrolyte velocity distribution of the electrolyte channel (b)

As shown in the images of the surfaces in Figs. 14 and 15, the work-pieces of the GH4169 alloy manufactured by ECM are more dramatically affected by turbulent eddies in the sodium chloride electrolyte. A possible explanation for this is that the volume expansion ratio of anodic products generated in sodium chloride electrolyte is higher than that in sodium nitrate electrolyte, which contributes to thicker layer of anodic products in electrolyte. As the electrolytic reaction continues in sodium chloride electrolyte, the amount of anodic products accumulated in the high-dissipation region and the low Reynolds number region are greater than that of the sodium nitrate electrolyte, thus the

electrolysis velocity of anode are lower in these region. Moreover, the electrolysis velocity of anode is higher in the low-dissipation region, because the concentrated electrolyte flux removes metal oxides in this region. Therefore, in sodium chloride electrolyte, the anode surface will become uneven. However, in sodium nitrate electrolyte, the process is quite different because of thinner layer of anodic products, which is more easily removed by electrolyte flux; thus, the difference of electrolysis velocity among high-dissipation region, low-dissipation region and low Reynolds number region disappears, and the anode surface will be still flat. This indicates that GH4169 alloy manufactured by means of ECM with sodium nitrate electrolyte will be of better processing quality than that prepared in sodium chloride electrolyte.

4. CONCLUSIONS

Compared to measurement under conditions of free convection, the electrochemical dissolution characteristics of GH4169 measured under ECM conditions differ significantly, including a reduction of E_{COP} and the improvement of the electron transfer process at the work-piece surface and ion diffusion from the work-piece to the electrolyte. In addition, when the electrolyte is under high-speed flow in both sodium chloride and sodium nitrate electrolytes, the current densities are similar, although they differ greatly in the state of free convection; furthermore, pre-passivation regions are not present after the decomposition potential, whereas both exist in these two electrolytes in the state of free convection. This investigation shows that electrolyte flow is conducive to electrochemical machining, increasing the current density, and, as the electrolyte velocity increases, the current density increases. Under ECM conditions, when the anode potential is greater than the decomposition potential and electrochemical machining occurs, the current density exponentially increases with increasing anode potential at the beginning of the potential and is linearly and positively correlated with the anode potential at later potentials. In addition, the cause of the sunken regions on the work-piece surface in sodium chloride electrolyte have been discussed and are attributed to higher volume expansion ratio of the anodic products and the different dissipation of the turbulent eddies in the distinct regions of the electrode surface; thus, the sodium nitrate electrolyte has better processing qualities than the sodium chloride electrolyte.

ACKNOWLEDGEMENTS
The authors acknowledge the financial support of Key Research & Development Plan of Jiangsu Province (BE2015160) and the Fundamental Research Funds for the Central Universities (NE2014104). Besides, authors thank to Mr. Zhongdong Fang of NUAA for his collaboration in the pre-processing of anode electrodes.

References

1. O. Ozgun, R. Yilmaz, H.O. Gulsoy, F. Findik, *Materials Characterization*, 108 (2011) 8
2. O. Ozgun, H.O. Gulsoy, R. Yilmaz, F. Findik, *Journal of Alloys and Compounds*, 546 (2013) 192

3. O. Ozgun, H.O. Gulsoy, F. Findik, R. Yilmaz, *Powder Metallurgy and Metal Ceramics*, 55 (2012) 405
4. S.L. Soo, R. Hood, D.K. Aspinwall, W.E. Voice, C. Sage, *CIRP Annals-Manufacturing Technology,* 60 (2011) 89
5. F. Klocke, M. Zeis, A. Klink, *Key Engineering Materials*, 504 (2012) 1237
6. F. Klocke, M. Zeis, A. Klink, D. Veselovac, *Procedia CIRP*, 6 (2013) 369
7. K.P. Rajurkar, D. Zhu, J.A. Mcgeough, J. Kozak, A. DeSilva, *CIRP Ann*. 48 (1999) 567
8. Z.Y. Xu, Q. Xu, D. Zhu, T. Gong, *CIRP Ann.*, 62 (2013) 187
9. G.M. Lin, H.Z. Cai, *Advanced Materials Research* ,472–475 (2012) 875
10. Osami Seri, Yoshiki Itoh, *Electrochimica Acta*, 218 (2016) 345
11. Bekenova Gulmira, Baeshov Abduali,Yılmaz Satılmış, *Oriental Journal of Chemistry*, 31 (2015) 141
12. O. Dagdag, A. Essamri , A. El Harfi, M. Galai, M. Ebn Touhami, *Journal of Materials and Environmental Science*, 7 (2016) 3454
13. A.R. Mount, P.S. Howarth, D. Clifton, *Journal of The Electrochemical Society*, 150 (2003) 63
14. A.R. Mount, K.L. Eley, D. Clifton, *Journal of Applied Electrochemistry*, 30 (2000) 447
15. Ching An Huang, Yu Chen Chen, *Corrosion Science*, 51 (2009) 1901
16. Dengyong Wang, Zengwei Zhu, Ningfeng Wang, Di Zhu, Hongrui Wang, *Electrochimica Acta.* 156 (2015) 301 [17] M. Burger, L. Koll, E.A. Werner, A. Platz, *Journal of Manufacturing Processes*, 14 (2012) 62
17. Qu N.S, Zhang Q.L, Fang X.L, Ye E.K, Zhu D, *Procedia CIRP*, 35 (2015) 16
18. Abhishek Singh, S. Anandita, and S. Gangopadhyay, *Materials and Manufacturing Processes*, 30 (2015) 842
19. G.L. Wynick, C.J. Boehlert, *Materials Characterization*, 55 (2005) 190
20. M.Kalaimathi, G.Venkatachalam, M.Sivakumar, *Jordan Journal of Mechanical and Industrial Engineering*, 8 (2014) 143
21. Zhouzhi Gu, Dong Zhu, Tingyu Xue, Ao Liu, Di Zhu, *International Journal of Advanced Manufacturing Technology*, 89 (2017) 877
22. N. K. Jain, A. Potpelwar, Sunil Pathak, N. K. Mehta, *International Journal of Advanced Manufacturing Technology*, 85 (2016) 2083
23. Martin Weinmann, Moritz Stolpe, Olivier Weber, Ralf Busch, Harald Natter, *Journal of Solid State Electrochemistry*, 19 (2015) 485
24. Hoshikawa, T, Yamada, M, Kikuchi, R, Eguchi, K, *Journal of Electroanalytical Chemistry*, 577 (2005) 339
25. Allen J. Bard , Larry R. Faulkner, "Electrochemical Methods: Fundamental and Applications, 2nd Edition", *John Wiley & Sons, Inc.*,(2001) 605 Third Avenue, New York
26. Stephan R. de Roode, Harm J. J. Jonker, Bas J. H. van de Wiel, Victor Vertregt, Vinvet Perrin, *Journal of the atmospheric sciences*, 74 (2017) 1495
27. Ann E. Gargett, *Journal of Atmospheric and Oceanic Technology*, 34 (2017) 1387
28. C.A. Huang , Y.C. Chen, J.H. Chang, *Corrosion Science*, 50 (2008) 480